Research Article Vol. 62, No. 17 / 10 June 2023 / Applied Optics 4635

# Double-ring-disk hybrid nanostructures with slits for electric field enhancement

Haiwei Mu,[1] Xinchen Xu,[1] Jingwei Lv,[1,*] Chao Liu,[1] Wei Liu,[1] Lin Yang,[1] Jianxin Wang,[1] Qiang Liu,[1] Yan Lv,[1] and Paul K. Chu[2]

[1]School of Physics and Electronic Engineering, Northeast Petroleum University, Daqing 163318, China
[2]Department of Physics, Department of Materials Science and Engineering, and Department of Biomedical Engineering, City University of Hong Kong, Tat Chee Avenue, Kowloon, Hong Kong, China
*msm-liu@126.com

Received 9 March 2023; revised 22 April 2023; accepted 24 April 2023; posted 26 April 2023; published 5 June 2023

**Although noble metal nanoantennas have distinctive optical properties and local electric field enhancement, considerable non-radiative ohmic losses occur at the optical frequencies, consequently creating significant absorption and unwanted heating. Combining the plasmon mode of metal nanoantennas with the anapole mode of high refractive index dielectric materials offers a promising alternative to increase the electric field strength with minimal loss. Herein, a silicon disk with slots and two Au rings with a coupling mechanism are described. To elucidate the field enhancement mechanism, the near-field enhancement features and near-field electric field distributions are explored by a numerical simulation and multipole decomposition analysis. By opening the slit to generate high-intensity hot spots inside the disk, the electric field can be enhanced significantly, and nearby molecules can directly contact these hot spots. The resulting large field enhancement suggests significant applications to strong photon-exciton coupling and nonlinear photonics.** 

https://doi.org/10.1364/AO.489456

## 1. INTRODUCTION

With the advent of metamaterials and transformation optics, plasmonic applications have grown significantly in recent years, leading to the emergence of novel physical phenomena and device applications in advanced optics and optoelectronics [1,2]. Among them, controlling and manipulating light on the microscale and nanoscale is one of the challenging issues [3]. In fact, owing to the significant field enhancement and tiny module volume, metal plasma nanostructures have received a lot of attention in the last decade. These structures not only produce resonance modes with subwavelength field limitation, known as local surface plasmon resonance (LSPR), but also produce strong light matter interactions. However, the non-irradiation ohmic loss of noble metal nanostructures of pure metals such as gold and silver is quite high at the optical frequencies, consequently causing significant absorption and undesirable heating [4]. Since efficient control of nano-level visible light is essential to future light-on-chip integration, optical information processing, and other technologies, the non-irradiation ohmic losses and thermal effects are show stoppers for pure metal nanostructures and have significant negative impacts on the overall performance, as well as universality and development. In order to address these drawbacks, dielectric nanostructures with similar resonance properties, high refractive indices, low loss, and capacity to support electric and magnetic resonance at optical frequencies are suitable alternatives [1,5] and semiconductors such as Si, Ge, and GaP constitute a more flexible class of plasmonic materials [6].

Under visible light irradiation, the nanoantenna can compress the optical energy into a volume less than the diffraction limit due to LSPR effects [7,8], and this process creates a substantially enhanced local electric field (a "hot spot") in the vicinity of the metallic nanoantenna arising from LSPR [9,10]. The high-intensity electric field enhancement bodes well for a variety of nanophotonic technologies, including surface-enhanced Raman scattering [11], surface-enhanced fluorescence emission (SEF) [12], augment surface-enhanced infrared absorption (SEIRA) [13–15], photothermal biosensing [16], and nano-lasing [17]. Therefore, it is necessary to promote near-field augmentation of nanoantennas, since it is essential to the development of nanophotonics. To improve the near-field electric field, several strategies have been proposed, for example, the nanoantenna structure with a tailored complex geometry [18], surface morphology [19], or creation of two symmetrical plasma metal nano-dimer structures with a short distance. Even though there has been some advancement in the field strength factor, it is still crucial to achieve low loss. Silicon is the suitable replacement for high refractive index dielectric nanomaterials due to the universal nature and simple processing of semiconductor devices. Silicon nanophotonics are numerous and diverse, including waveguides (discrete, unidirectional

without energy loss, etc.) [20,21], modulators [22], directional light sources of directional light sources [23], detectors, and phase super surfaces [24]. In this work, a hybrid structure consisting of metal and high refractive index dielectric materials is designed for a high local electric field enhancement. The nanostructures with a metal nanoring and silicon nanodisk are investigated before integrating the two structures and a structure in which the two rings and a disk overlap are created. The use of high refractive index dielectric materials significantly lowers non-irradiation ohmic losses while maintaining the plasma resonance properties of metals. The anapole mode response was improved, achieving an ultra-strong electric field augmentation.

The electric field intensity ($|E_{max}/E_0|$) peak is about 10 and about three times that of a single disk. A slit is cut in the middle of the disk, and the hybrid dielectric metal nanoantenna's electric field augmentation is investigated for various settings in order to advance our understanding of the electric field enhancement mechanism. In the manufacturing process during production, we can fabricate our structure by employing the conventional nanofabrication and thin film deposition processes.

## 2. MULTIPOLE COMPOSITION METHOD

The finite element method based on the commercial COMSOL Multiphysics software is implemented in the numerical simulation. The boundary conditions of the matched layer are applied to the nanostructures in a vacuum. The refractive index of the dielectric slab is set to 3.5, and Au is taken from Palik's handbook [25]. The surrounding index for the simulation is $n = 1$.

Different multistage modes are calculated, and their contribution to the scattering spectrum can be ascertained using the multistage decomposition approach which includes electric dipole moment $P_\alpha$ (ED), magnetic dipole moment $M_\alpha$ (MD), toroidic dipole moment $T_\alpha$ (TD), electric quadrupole moment $Q^e_{\alpha\beta}$ (EQ), and magnetic quadrupole moment $Q^m_{\alpha\beta}$ (MQ) as follows [26,27]:

$$P_\alpha = \frac{1}{i\omega}\int J_\alpha \mathrm{d}^3 r, \tag{1}$$

$$M_\alpha = \frac{1}{2c}\int [r \times J]_\alpha \mathrm{d}^3 r, \tag{2}$$

$$T_\alpha = \frac{1}{10c}\int [(r \cdot J) r_\alpha - 2r^2 J_\alpha] \mathrm{d}^3 r, \tag{3}$$

$$Q^e_{\alpha\beta} = -\frac{1}{i\omega}\int \left[r_\alpha J_\beta + J_\alpha r_\beta - \frac{2}{3}\delta_{\alpha\beta}(r \cdot J)\right] \mathrm{d}^3 r, \tag{4}$$

$$Q^m_{\alpha\beta} = \frac{1}{3c}\int \left[[r \times J]_\alpha r_\beta + r_\alpha [r \times J]_\beta\right] \mathrm{d}^3 r, \tag{5}$$

where $j$ denotes the polarization current density excited in the antenna, $r$ is the distance vector, and the subscripts $\alpha, \beta = x, y, z$ denote the components of EQ and MQ. The radiation power $I$ of these different multipole moments can be derived as follows [28]:

$$I = \frac{1}{8\pi\varepsilon_0}\left[\frac{2\omega^4}{3c^3}|P|^2 + \frac{2\omega^4}{3c^3}|M|^2 + \frac{4\omega^5}{3c^4}\mathrm{Im}(P^* T) + \frac{2\omega^6}{3C^5}|T|^2 + \frac{\omega^6}{20c^5}\sum |Q^e|^2 + \frac{\omega^6}{20c^5}\sum |Q^m|^2\right]. \tag{6}$$

The total scattering cross section can be approximated as

$$C_{sca} = \frac{I}{I_{inc}}, \tag{7}$$

where $I_{inc}$ is the radiation power of the incident light wave. The near-field electric field intensity enhancement is calculated by the following formula:

$$\mathrm{NI} = (E/E_0) = \left(\sqrt{E_{ex}^2 + E_{ey}^2 + E_{ez}^2}\right)/E_0, \tag{8}$$

where $E_0$ represents the incident electric field intensity, which equals 1 V/m.

## 3. RESULTS AND DISCUSSION

The optical properties of a single ring structure are shown in Fig. 1. Gold nanoparticles have a wide range of applications in the field of nanoantennas due to their distinctive physical characteristics. Au nanoparticles are highly biocompatible, non-oxidizing, and chemically inert when compared to materials such as silver and copper [29]. We choose Au as the material and dielectric functions extracted from Palik's handbook, and the index of the surrounding medium is taken to be 1. A numerical simulation is carried out using commercial COMSOL software. Figure 1(a) shows the scattering cross sections of the Au ring. The inner and outer radii of the gold ring are $R_{in} = 390$ and $R_{out} = 490$ nm, respectively. The Au ring is excited by a normal incident plane wave and irradiated with $y$-polarized light. A peak appears at a wavelength of 1103 nm in the scattering spectrum. In order to understand this peak in the scattering spectrum, we calculate the contributions from different multipole modes to the spectrum, as shown in Fig. 1(b). It is clear that the peak at 1103 nm originates from the electric dipole (ED) and TD. Moreover, the ED is dominant throughout the spectrum and the contributions of the EQ and MQ are negligible. The electric near-field distribution profile of the ring on the $x$-$y$ plane ($x = 0$) is calculated at the resonance wavelength of $\lambda = 1103$ nm, as shown in Fig. 1(c). The electric field of the golden ring exhibits an outstandingly symmetrical distribution. The electric field enhancement caused by dipole resonance is symmetrically concentrated on both sides of the ring, and the red arrow representing the current direction also forms a subtle loop on both sides. There is a significant enhancement of the electric field on the ring, and this field distribution is very important to strong coupling of the disk-ring structure.

The refractive index of the Si nanodisk is set to $n = 3.5$, and the height and bottom radii of the nanodisk are 100 and 230 nm. To reveal the anapole modes governed by the disk, the contributions from different multipole modes to the scattering spectrum of the nanodisk are shown in Fig. 2(a). An obvious resonance dip can be found around $\lambda = 974$ nm revealing the excited anapole mode. This results from the electric dipole and ring dipole interference and interplay, which creates a zero point

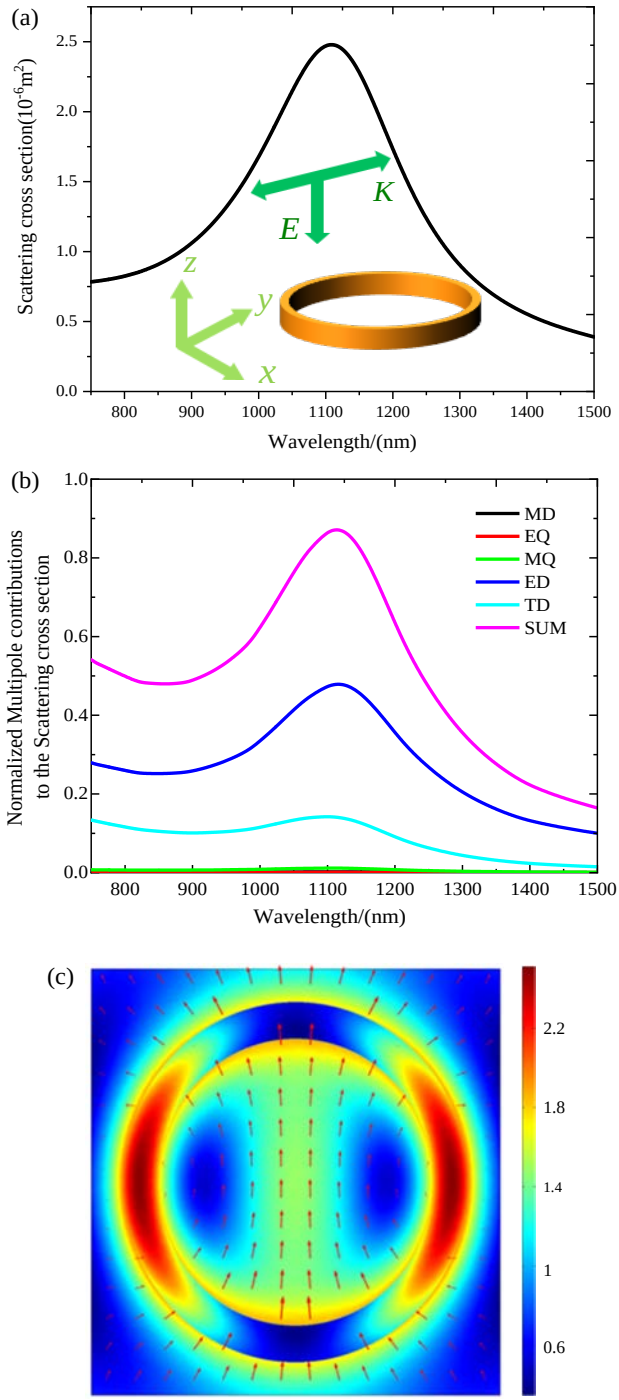


**Fig. 1.** Optical responses of a single ring. (a) Scattering spectrum of the gold ring with a height of 100 nm. The inset shows the schematic of the structure with plane wave excitation, and the origin of the coordinate system is placed at the center of the ring. (b) Contributions from different multipole modes to the scattering spectrum of the individual ring: ED, MD, TD, EQ, and MQ. The MD contribution approaches 0 and is covered by the red line. (c) Near-field profiles on the $z = 0$ plane of the ring. The wavelength is $\lambda = 1103$ nm.

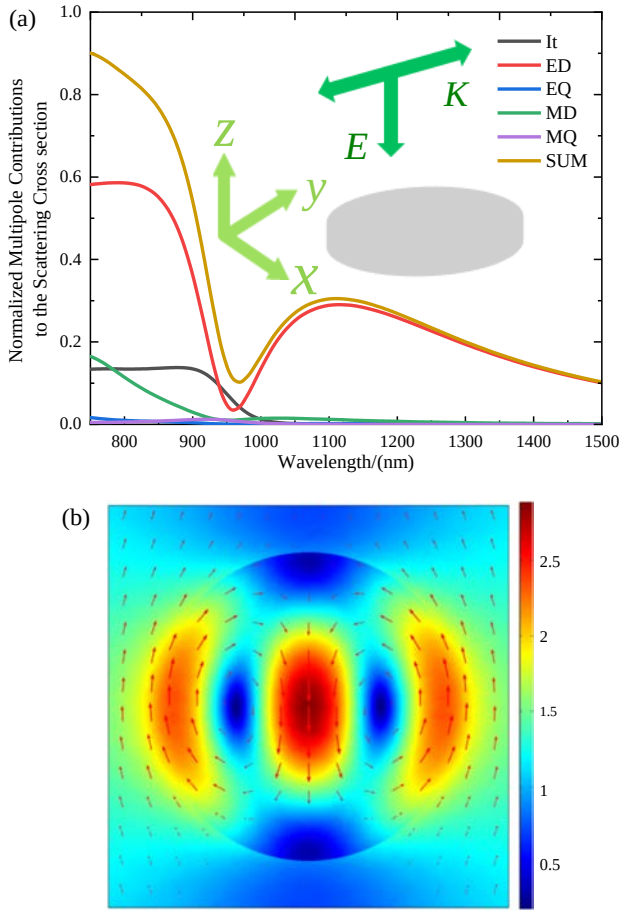


**Fig. 2.** Optical responses of a single disk. (a) Contributions from different multipole modes to the scattering spectrum of the individual disk and (b) near-field profiles on the $z = 0$ plane at $\lambda = 974$ nm with the dashed line showing the edge of the disk.

and causes a wave valley to emerge [30]. ED and TD contribute significantly to the scattering cross section, which is an electric dipole state [31]. The inset shows the schematic of the structure, and the origin of the coordinate system is placed in the center of the nanodisk. Figure 2(b) shows the electric field distribution on the $z = 0$ plane. Similar results have been reported [32–35]. The direction of the electric field flow is shown by the red arrow on the surface. A closed loop is visible in the electric field arrows inside the disk, which shows a circular model with steady polarized surface currents. This also implies that a classic anapole mode has emerged [30].

The optical responses of the coupled system that consist of the Si nanodisk and Au ring as are shown in Fig. 3. Figure 3(a) shows the schematic of the coupled system under plane wave illumination. Here there are two configurations of the Si disk and Au ring: a single disk and ring (top right) and a single disk with two rings (bottom right). The incident wave is polarized along the $y$ axis, and the origin of the coordinate system is placed at the center of the ring. The first type of disk is positioned at (0, 0, 100 nm), which is 100 nm above the ring center. The bottom of the second type is the same as the bottom of the first type, with an additional ring placed on top to create a symmetrical structure. The index of the surrounding medium is also 1. Figures 3(b) and 3(c) depict the surface charge distributions of the first type and second type coupling structures at incident wavelengths of 925 and 937 nm, respectively. We select both the upper surface of the lower ring and lower surface of the disk. The induced charges are distributed on the surface of the disk and

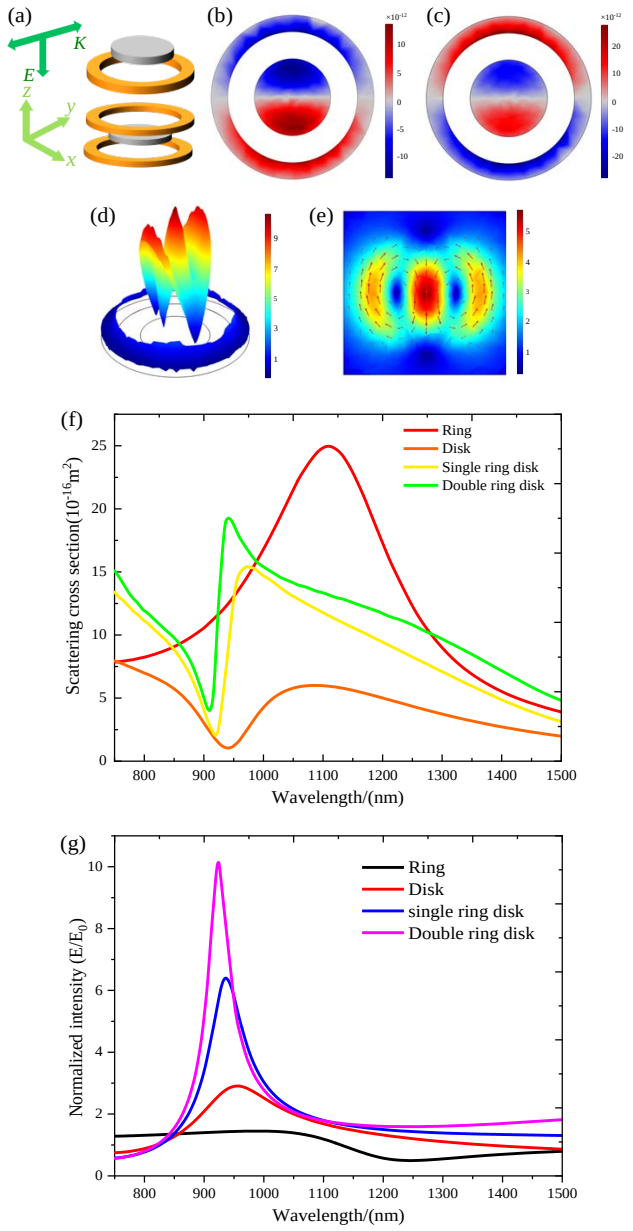


**Fig. 3.** Optical responses of the coupled system of a disk of Si and Au rings. (a) Schematic of the coupled system under plane wave incident illumination; (b) surface charge distribution of the first type at the incident wavelength of 925 nm; (c) surface charge distribution of the second type coupling structures at the incident wavelength of 937 nm; (d) second structure distribution of the electric field in three dimensions; (e) near-field profiles on the $z = 150$ plane at $\lambda = 926$ nm of the second type of structure; (f) comparison of the scattering spectra of the ring disk coupling system; (g) near-field enhancement of the ring, disk, and coupling system.

ring with positive and negative charges represented by red and blue, respectively. The positive and negative charges are evenly distributed on both sides of the disk with clear boundaries. The charge density distribution reveals that the peak value of the anapole corresponds to the dipole resonance mode. Since the electric field distribution diagrams of the two coupling systems are relatively similar and the effect of the second type of coupling system is obviously better than that of the first type after calculation, only the three-dimensional electric field distribution diagram and plane near-field electric field distribution of the double-ring-disk coupling structure are shown in Figs. 3(d) and 3(e), respectively. In order to gain insight into the electric field enhancement effects of the coupled system, the intensity enhancement curves of the Au ring antenna (red solid line) and Si disk (orange solid line), as well as the single ring disk (green solid line) and double ring disk (yellow solid line) are shown in Fig. 3(d) (green solid line). These significant peaks correspond to the wave trough position in the scattering spectrum. Figure 3(e) displays the Au ring, Si disk, and two types of coupling system electric field strength enhancement curves. The first coupling system antenna exhibits a near-field augmentation that is two times greater than that of the disk antenna, while the second one is improved 3.5 fold.

The enhanced anapole response indicates that a large electric field enhancement can be achieved in this system by introducing a small slot in the disk [36,37]. Although the small slot effect on the coupling system electric field enhancement is not obvious, it can be improved by altering the slot size and form. The significant improvements observed can be attributed to the excitation of a hybrid plasmon that involves extensive localized charge distributions of the opposite sign on both sides of the gap. This is similar to the dipolar bonding dimer plasmons that are present in nanoparticle dimers [38]. Additionally, the groove may facilitate easy contact between the enhanced electric field and other objects. We select the second kind of coupling system with a greater electric field enhancement effect. On its disk, we made a small cuboid gap and calculated the contributions from different multipole modes to the scattering spectrum of the hybrid nanostructures, as shown in Fig. 4. The internal illustration shows the structural diagram of the hybrid structure. As shown in Fig. 4(b), we intercept the surface charge distribution of the disk assembly at a wavelength of 862 nm. It is obvious that a large number of dense positive and negative charges are covered on both sides of the gap. The charge density on the disk assembly surface is an order of magnitude higher than that in a connected system with no gaps. The generation of a dipole resonance mode generates a well-defined distribution of positive and negative charges on both sides. Figure 4(c) shows the three-dimensional electric field diagram of the slotted coupling structure. Most of the energy is contained in the cuboid slit, as indicated by the electric field distribution diagram of Fig. 4(c), where practically all the fields circulate in the disk plane. The field enhancement factor is the highest at 82.4. The charge distribution at the cuboid gap opening displays a dipole distribution when the wavelength is 862 nm. The superiority of this coupling system is demonstrated by the high concentration of positive and negative charges on each side of the gap, as well as outstanding electric field amplification.

Next, we investigate the influence of the geometrical features of the tiny grooves on the variation of the electric field enhancement. A contour map is made in the correlation function curve, as shown in Fig. 5. Increasing the cuboid gap length $L$ causes the wave peak to gradually rise, producing a noticeable blueshift, as shown in Fig. 5(a), before the length is less than 160 nm. When the wavelength is more than 160 nm, the wave peak rises noticeably and tends to remain steady until a wavelength of $L = 260$ nm, where the maximum is attained. The electric field enhancement factor is 82.4 at this point, but a tiny decline in the peak value follows, albeit not immediately apparent. In

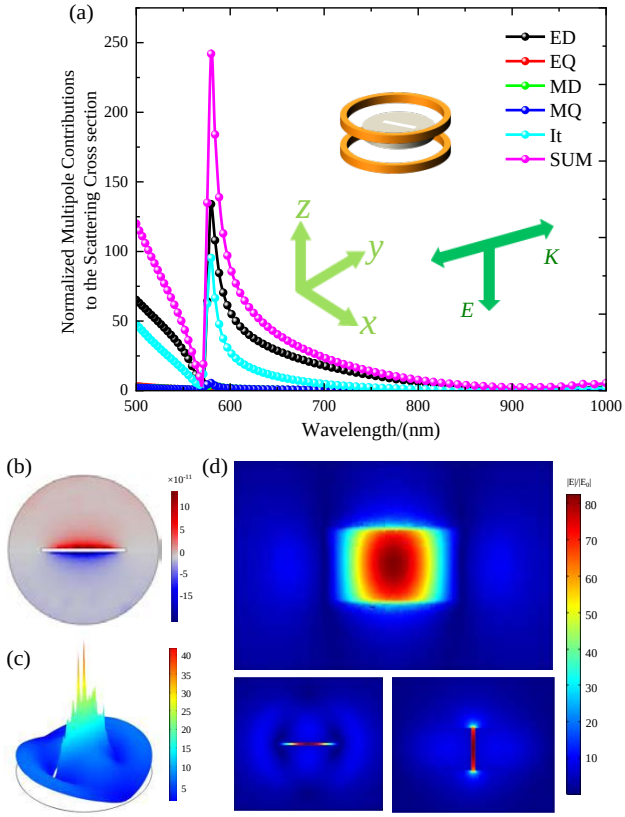


**Fig. 4.** (a) Contributions from different multipole modes to the scattering spectrum of the coupling system with the slit; (b) surface charge distribution of the disk portion at an incident wavelength of 862 nm; (c) three-dimensional electric field diagram of the slotted coupling structure; (d) electric field distributions in the *x*-*z* plane, *x*-*y* plane, and *y*-*z* plane.

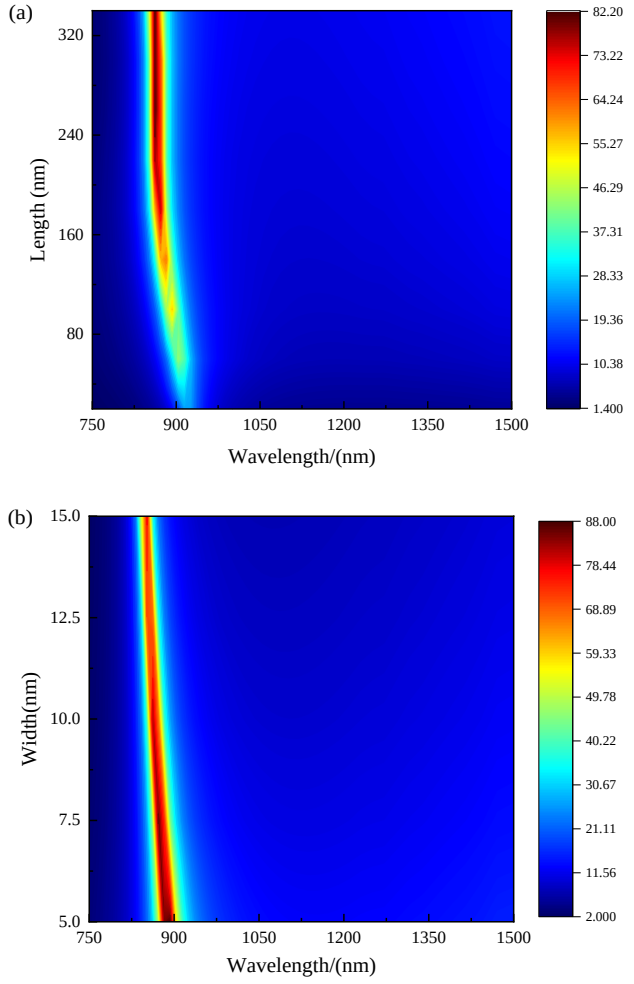


**Fig. 5.** Size-dependent near-field intensity enhancement of the cuboid gap: (a) effects of the gap length, H, on the intensity enhancement spectra and (b) effects of the gap width, W, on the intensity enhancement spectra.

contrast to Fig. 5(a), Fig. 5(b) demonstrates that as the width W is reduced, the wave peak redshifts, and the peak value likewise rises. The electric field enhancement factor reaches 88 when the slot width is 5 nm. Obviously, the electric field augmentation effect improves as the slit narrows. The subsequent analysis is performed for a width of 10 nm due to the experimental circumstances and convenience of contact with other objects.

The influence of the changing ring geometric parameters on the electric field enhancement and resonance wavelength is shown in Figs. 6(a)–6(c) with other coupling system parameters unchanged. Figure 5(a) shows the results of different Au ring sizes, where $R_{out} - R_{in}$ is limited to 100 nm in each case. The best electric field enhancement is found at $R_s = 480$ nm, and the electric field enhancement factor is 92.4. This can be explained as follows. By increasing the ring size, the optical response of the ring increases. The resonance position is far from the operating wavelength, and the distance between the disk and the ring also increases. The combination of these factors produces the optimal phenomenon, which is similar to the phenomenon in Figs. 5(b) and 5(c). Another significant factor determining the field enhancement value is the geometric shape of the ring. The effects of the inner and outer radii are investigated as shown in Figs. 5(b) and 5(c), respectively. When the inner radius is $R_{in} = 390$ nm in Fig. 5(b), the outer radius increases from 450 to 510 nm. The resonance electric field enhancement reveals an ideal value close to $R_{out} = 500$ nm. The impact of increasing the inner radius from 360 to 400 on the amplification of the electric field is illustrated in Fig. 5(c). Similarly, the outer radius remains unchanged at 490. At this point, the resonant electric field enhancement is found to be 93.2 at $R_{in} = 380$ nm. Finally, we compare it with the conventional slotted silicon disk nanoantenna and single ring disks with slit nanostructures in Fig. 5(d) to demonstrate the effects on the electric field enhancement. Obviously, the effects rendered by the slotted double-disk-ring coupling system are significantly better than those of the classical slotted nanodisk. In the experiments, the form and size of the slit, disk, and ring have some variability and these parameters affect the near-field electric field enhancement, as demonstrated by the systematic simulation results.

## 4. CONCLUSION

A high-performance hybrid metal dielectric nanostructure is designed to enhance the resonant electric field. Based on the traditional ring and disk, the hybrid system is constructed with a rectangular groove in the disk to increase the electric field by

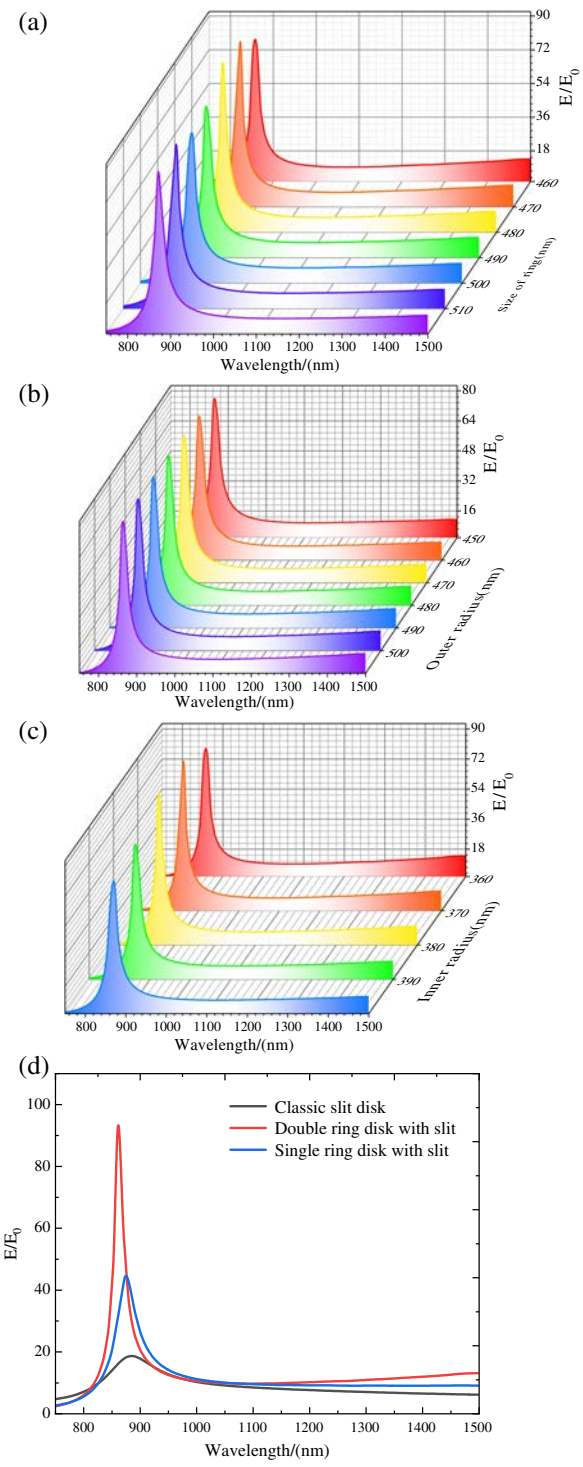


**Fig. 6.** (a) Resonant electric field enhancement as a function of the outer radius of the ring with $R_{out}$-$R_{in}$ fixed at 100 nm for all the rings; (b) resonance electric field enhancement with changes of the outer radius of the ring; (c) resonance electric field enhancement with changes of the inner radius of the ring; (d) electric field enhancement of circular disks with slits and single ring disks with slit nanostructures, as well as double ring disks with slit nanostructures.

nearly 100 times. The basic optical response of the system is analyzed by the multipole decomposition method, and the effects of the geometric parameters and modal interactions on the spectral evolution and intensity enhancement are studied. By analyzing the two factors that affect the spectral evolution and intensity enhancement and comparing them with the classical slotted disk, the electric field enhancement of the disk-ring coupling slotted system is found to be about 10 times. Electromagnetic resonance at a high electric field is expected to spur applications in sensing, nanoantennas, and nanophotonics, and offers excellent guidance for diverse photonic applications that require high-field-density light-matter interactions.

**Funding.** City University of Hong Kong Donation Research Grant (9229021) and Strategic Research Grant (SRG) (7005505); China Postdoctoral Science Foundation (2020M670881); Local Universities Reformation and Development Personnel Training Supporting Project from Central Authorities, Natural Science Foundation of Heilongjiang Province (LH2021F007); Outstanding Young and Middle-Aged Research and Innovation Team of Northeast Petroleum University (KYCXTD201801).

**Disclosures.** The authors declare no conflicts of interest.

**Data availability.** Data underlying the results presented in this paper are not publicly available at this time but may be obtained from the authors upon reasonable request.

## REFERENCES

1. G. V. Naik, V. M. Shalaev, and A. Boltasseva, "Alternative plasmonic materials: beyond gold and silver," Adv. Mater. **25**, 3264–3294 (2013).
2. W. Liu, C. J. Hu, L. Zhou, Z. Yi, C. Liu, J. W. Lv, L. Yang, and P. K. Chu, "A square-lattice D-shaped photonic crystal fiber sensor based on SPR to detect analytes with large refractive indexes," Phys. E **138**, 115106 (2022).
3. U. Zywietz, A. B. Evlyukhin, C. Reinhardt, and B. N. Chichkov, "Laser printing of silicon nanoparticles with resonant optical electric and magnetic responses," Nat. Commun. **5**, 3402 (2014).
4. P. B. Johnson and R. W. Christy, "Optical constants of the noble metals," Phys. Rev. B **6**, 4370–4379 (1972).
5. Q. Zhao, J. Zhou, F. Zhang, and D. Lippens, "Mie resonance-based dielectric metamaterials," Mater. Today **12**(12), 60–69 (2009).
6. A. Hryciw, Y. C. Jun, and M. L. Brongersma, "Electrifying plasmonics on silicon," Nat. Mater. **9**, 3–4 (2010).
7. M. Agio and A. Alù, *Optical Antennas* (Cambridge University, 2013).
8. P. Albella and S. A. Maier, "Unidirectional light scattering with high efficiency at optical frequencies based on low-loss dielectric nanoantennas," Nanoscale **8**, 14184 (2016).
9. H. Sugimoto and M. Fujii, "Broadband dielectric-metal hybrid nanoantenna: Silicon nanoparticle on a mirror," ACS Photonics **5**, 1986–1993 (2018).
10. W. Liu, F. M. Wang, C. Liu, *et al.*, "A hollow dual-core PCF-SPR sensor with gold layers on the inner and outer surfaces of the thin cladding," Results Opt. **1**, 100004 (2020).
11. X. Shi, N. Coca-López, J. Janik, and A. Hartschuh, "Advances in tip-enhanced near-field Raman microscopy using nanoantennas," Chem. Rev. **117**, 4945–4960 (2017).
12. R. Regmi, A. A. Al Balushi, H. Rigneault, R. Gordon, and J. Wenger, "Nanoscale volume confinement and fluorescence enhancement with double nanohole aperture," Sci. Rep. **5**, 15852 (2015).
13. F. Neubrech, C. Huck, K. Weber, A. Pucci, and H. Giessen, "Surface-enhanced infrared spectroscopy using resonant nanoantennas," Chem. Rev. **117**, 5110–5145 (2017).
14. W. Liu, C. Liu, J. X. Wang, J. W. Lv, Y. Lv, L. Yang, N. An, Z. Yi, Q. Liu, C. J. Hu, and P. K. Chu, "Surface plasmon resonance sensor composed of microstructured optical fibers for monitoring of external and internal environments in biological and environmental sensing," Results Phys. **47**, 106365 (2023).
15. L. V. Brown, X. Yang, K. Zhao, B. Y. Zheng, P. Nordlander, and N. J. Halas, "Fan-shaped gold nanoantennas above reflective substrates for surface-enhanced infrared absorption (SEIRA)," Nano Lett. **15**, 1272–1280 (2015).

16. P. Zijlstra, P. M. R. Paulo, and M. Orrit, "Optical detection of single non-absorbing molecules using the surface plasmon resonance of a gold nanorod," Nat. Nanotechnol. **7**, 379–382 (2012).
17. R. F. Oulton, V. J. Sorger, T. Zentgraf, R. M. Ma, C. Gladden, L. Dai, G. Bartal, and X. Zhang, "Plasmon lasers at deep subwavelength scale," Nature **461**, 629–632 (2009).
18. X. Cui, Y. Lai, R. Ai, R. Ai, H. Wang, L. Shao, H. Chen, W. Zhang, and J. Wang, "Anapole states and toroidal resonances realized in simple gold nanoplate-on-mirror structures," Adv. Opt. Mater. **8**, 2001173 (2020).
19. Y. Wang, P. Zhang, W. Fu, and Y. Zhao, "Morphological control of nanoprobe for colorimetric antioxidant detection," Biosens. Bioelectron. **122**, 183–188 (2018).
20. R. S. Savelev, D. S. Filonov, M. I. Petrov, A. E. Krasnok, P. A. Belov, and Y. S. Kivshar, "Resonant transmission of light in chains of high-index dielectric particles," Phys. Rev. B **92**, 155415 (2015).
21. W. Liu, Z. Shi, Z. Yi, C. Liu, F. M. Wang, X. L. Li, J. W. Lv, L. Yang, and P. K. Chu, "Surface plasmon resonance chemical sensor composed of a microstructured optical fiber for the detection of an ultra-wide refractive index range and gas-liquid pollutants," Opt. Express **29**, 40734 (2021).
22. O. Limona, L. Businarob, A. Gerardinoc, L. Bittond, A. Frydmand, and Z. Zalevskya, "Fabrication of electro optical nano modulator on silicon chip," Microelectron. Eng. **86**, 1099–1102 (2009).
23. A. E. Krasnok, A. E. Miroshnichenko, P. A. Belov, and Y. S. Kivshar, "All-dielectric optical nanoantennas," Opt. Express **20**, 20599–20604 (2012).
24. D. Lin, P. Fan, E. Hasman, and M. L. Brongersma, "Dielectric gradient metasurface optical elements," Science **345**, 298–302 (2014).
25. E. D. Palik, *Handbook of Optical Constants of Solids* (Academic, 1985).
26. X. Zhang, Q. Zhang, Y. Yuan, J. Liu, and X. Liu, "Ultra-directional forward scattering by a high refractive index dielectric T-shaped nanoantenna in the visible," Phys. Lett. A **384**, 126696 (2020).
27. V. Savinov, V. A. Fedotov, and N. I. Zheludev, "Toroidal dipolar excitation and macroscopic electromagnetic properties of metamaterials," Phys. Rev. B **89**, 205112 (2014).
28. C. Xu, K. Cheng, Q. Li, X. Shang, C. Wu, Z. Wei, X. Zhang, and H. Li, "The dual-frequency zero-backward scattering realized in a hybrid metallo-dielectric nanoantenna," AIP Adv. **9**, 075121 (2019).
29. H. Kang, J. T. Buchman, R. S. Rodriguez, H. L. Ring, J. He, K. C. Bantz, and C. L. Haynes, "Stabilization of silver and gold nanoparticles: preservation and improvement of plasmonic functionalities," Chem. Rev. **119**, 664–699 (2018).
30. K. Baryshnikova, D. Smirnova, B. Luk'yanchuk, and Y. Kivshar, "Optical anapoles in nanophotonics and meta-optics," Adv. Opt. Mater. **7**, 1801350 (2019).
31. D. E. Aspnes and A. A. Studna, "Dielectric functions and optical parameters of Si, Ge, GaP, GaAs, GaSb, InP, InAs, and InSb from 1.5 to 6.0 eV," Phys. Rev. B **27**, 985–1009 (1983).
32. A. E. Miroshnichenko, A. B. Evlyukhin, Y. F. Yu, R. M. Bakker, A. Chipouline, A. I. Kuznetsov, B. S. Lukyanchuk, B. N. Chichkov, and Y. S. Kivshar, "Nonradiating anapole modes in dielectric nanoparticles," Nat. Commun. **6**, 8069 (2015).
33. C. Liu, J. W. Lv, W. Liu, F. M. Wang, and P. K. Chu, "Overview of refractive index sensors comprising photonic crystal fibers based on the surface plasmon resonance effect [Invited]," Chin. Opt. Lett. **19**, 102202 (2021).
34. E. A. Gurvitz, K. S. Ladutenko, P. A. Dergachev, A. B. Evlyukhin, A. E. Miroshnichenko, and A. S. Shalin, "The high-order toroidal moments and anapole states in all-dielectric photonics," Laser Photonics Rev. **13**, 1800266 (2019).
35. W. Liu, C. J. Hu, L. Zhou, Z. Yi, C. Liu, J. W. Lv, L. Yang, and P. K. Chu, "Ultra-sensitive hexagonal PCF-SPR sensor with a broad detection range," J. Mod. Opt. **67**, 1545–1554 (2020).
36. Y. Yang, V. A. Zenin, and S. I. Bozhevolnyi, "Anapole-assisted strong field enhancement in individual all-dielectric nanostructures," ACS Photonics **5**, 1960–1966 (2018).
37. J. Wu, F. Zhang, Q. Li, Q. Feng, Y. Wu, and L. Wu, "Strong field enhancement in individual Φ-shaped dielectric nanostructures based on anapole mode resonances," Opt. Express **28**, 570–579 (2020).
38. A. García-Martín, D. R. Ward, D. Natelson, and J. C. Cuevas, "Field enhancement in subnanometer metallic gaps," Phys. Rev. B **83**, 193404 (2011).